Heliyon 8 (2022) e10264

Contents lists available at ScienceDirect

Heliyon

journal homepage: www.cell.com/heliyon

Research article

Zr, La-dual doped silver niobate for photocatalytic degradation of dyes under visible light irradiation

Chun Mun Khor [a], Mohammad Mansoob Khan [a,*], Abuzar Khan [b], Mohd Yusuf Khan [b], Mohammad Hilni Harunsani [a]

[a] Chemical Sciences, Faculty of Science, Universiti Brunei Darussalam, Jalan Tungku Link, Gadong, BE 1410, Brunei Darussalam
[b] Interdisciplinary Research Center for Hydrogen and Energy Storage, King Fahd University of Petroleum & Minerals (KFUPM), Dhahran, 31261, Saudi Arabia

ARTICLE INFO

Keywords:
Silver niobate
Perovskites
Photocatalysts
Organic pollutants
Visible light irradiation
Zr, La-dual doped silver niobate

ABSTRACT

Sol-gel-assisted synthesis of silver niobate, 1%, 5%, and 10% Zr, La-dual doped silver niobates were carried out. Analysis done using XRD showed that increasing Zr and La dual doping caused the synthesized materials to adopt an $AgNbO_3$-like structure. This is also supported by FT-IR results. FESEM revealed that the silver niobate has a prism-like morphology while Zr, La-dual doped samples are irregular in shape. EDX mapping of the 10% Zr, La dual silver niobate confirmed the presence of Nb, Ag, Zr, and La metals. When compared with the silver niobate, the band gap energy of Zr, La-dual doped silver niobates are narrower, as shown by UV-Vis DRS measurements. It was revealed that dual doping of silver niobates with Zr and La has significantly improved the photocatalytic degradation of methylene blue (MB) and Rhodamine B (RhB) dyes. The 1% Zr, La-dual doped silver niobate showed the best photocatalytic results in terms of degrading MB while 10% Zr, La-dual doped silver niobate achieved the best performance when degrading RhB.

1. Introduction

Catalysts such as those made from carbon-based, metallic, and semiconducting materials are important ingredients for chemical industries [1]. These catalytic materials speed up reaction time, increase product yield and prevent the use of harsh reaction conditions which are difficult to achieve through conventional methods [2]. They are also known to be environmentally friendly, reusable, and efficient for use in reactions like organic synthesis [2]. Hence, they can be used to drive reactions for the purpose of resolving energy and environmental crisis [1].

Photocatalysts are a group of catalytic materials used to speed up chemical reactions upon absorption of light [3, 4, 5]. These reactions are useful in many different applications such as water-splitting, photovoltaics, and photocatalytic organic synthesis, which are still being investigated and reported up to this day [3, 4, 6]. Furthermore, photocatalysts are also used in the removal of organic pollutants from water [3, 7, 8]. During this process, light energy is used to generate oxidizing species such as $^{\cdot}OH$ and $^{\cdot}O_2^-$ [7, 9, 10]. In theory, these short-lived radicals are highly-oxidizing and can be used to break down many types of organic pollutants in water. The mechanisms of photocatalysis can be described in three steps [3, 11]: i. photogeneration of electron-hole pairs; ii. charge separation and migration of electron-hole pairs to the surface of the photocatalyst, and; iii. redox reactions on the photocatalytic surface (where free radicals will be formed).

Currently, the use of photocatalysts in water treatment is very limited in industries [11, 12]. The source of this is the inability of the process to remain cost- and time-effective when scaled up [11, 13]. For example, it was reported that there is a commercially available water treatment unit known as Purifics Photo-Cat [13]. However, this system has drawbacks such as the use of UV light and the increased cost due to the recovery of photocatalysts. As a result, it is commercialized for small-scale applications [13]. Therefore, improvements are to be made in order to allow photocatalytic technology to be commercialized.

Silver niobates ($AgNbO_3$, $AgNb_7O_{18}$, etc.) are oxide materials that possess useful ferroelectric properties due to their NbO_6 octahedra in the unit cells [14, 15]. These octahedra may also result in the promotion of charge carrier separation in silver niobates which benefits photocatalysis [16]. As such, silver niobates have been investigated for their plausible use in the photocatalytic degradation of organic dyes [16, 17, 18, 19]. Some silver niobates are visible light-active while others absorb UV light [16, 18]. $AgNbO_3$ is one of the visible light-active silver niobates which have been assessed for photocatalytic degradation of organic dyes [17]. It

* Corresponding author.
E-mail addresses: mmansoobkhan@yahoo.com, mansoob.khan@ubd.edu.bn (M.M. Khan).

https://doi.org/10.1016/j.heliyon.2022.e10264
Received 4 April 2022; Received in revised form 18 April 2022; Accepted 8 August 2022

is an orthorhombic perovskite and has many other applications such as energy storage and O_2 evolution [20, 21, 22]. Other niobate perovskites such as $KNbO_3$ and $NaNbO_3$ possess high band gap energies [23]. $AgNbO_3$, on the other hand, has a significantly lower band gap energy of approximately 2.8 eV [17]. The reason for the narrow band gap is due to the orbital hybridization between Ag 4*d* and O 2*p* [24].

There are several reports on A-site doping of $AgNbO_3$, where the perovskite was doped by ions with different ionic charges such as Sm^{3+}, Nd^{3+}, and Li^{+} [25, 26, 27]. In Sm-doping of $AgNbO_3$, a phase transition from antiferroelectric to paraelectric was observed due to the distortion of the lattice when Sm^{3+} ions of different sizes and charges were introduced [25]. It was shown that the dopant could improve the dielectric properties of $AgNbO_3$, which may be useful in energy storage applications [25]. Nd-doping can also improve the energy storage capability of $AgNbO_3$ [26]. According to the literature, the cause of this is due to its large breakdown electric field when Nd^{3+} was introduced [26]. Furthermore, the stretching of the lattice structure and the subsequent change in antiferroelectricity were also observed after the material was doped with Nd [26]. $AgNbO_3$ can also be doped with Li to improve the ferroelectricity of the material [27]. After doping the material with Li, its crystal structure was reported to have changed from orthorhombic to rhombohedral [27].

The Nb at the B-site of $AgNbO_3$ can also be replaced by other cations. Examples of such B-site dopants include Ta^{5+}, Sb^{5+}, and V^{5+} [28]. $AgNbO_3$ doped with these ions was prepared via the solid-state synthesis method [28]. The aims of their formation are to improve the electric transport, dielectric and ferroelectric properties of $AgNbO_3$ [28]. Muduli *et al.* reported that the crystal structure, particle morphology, and ferroelectric property changed when a different dopant is used [28]. This report showed that both A-site ad B-site dopants can influence the crystal structure of $AgNbO_3$. Therefore, these dopants may play an important role in improving photocatalysis by altering the structure and morphology of $AgNbO_3$.

Codoping or dual doping is the process where two or more dopants are simultaneously introduced into a semiconductor. There are several reports which have addressed the codoping of $AgNbO_3$ [29–31]. These materials were also synthesized with the intention to be used in energy storing technologies such as capacitors [29, 30, 31]. For instance, La/Mn-codoped $AgNbO_3$ fabricated through ceramic method contains La which occupied the A-site while Mn occupied both the A-site and B-site. Mn was able to occupy both at the same time because of its multiple oxidation states [29]. Other examples of $AgNbO_3$ codoping were Ca^{2+}/Ta^{5+} and Sm^{3+}/Ta^{5+}, where the rolling process and solid state methods were used, respectively [30, 31].

In this work, Zr and La were used as the dual dopants for the respective B- and A-sites of silver niobate. The aim of this report is to enhance the effectiveness of the photocatalyst in dye degradation by dual doping. The sol-gel method was used for the synthesis of silver niobate and Zr and La-dual doped silver niobate. In the other reported sol-gel synthesis of $AgNbO_3$, additional reagents like hydrogen peroxide (H_2O_2) and ethylenediamine ($C_2H_4(N_2)_2$) were used and required a long preparation time [32]. The current method of synthesis, in contrast, does not require such reagents and has a relatively shorter preparation time. Also, unlike the sol-gel synthesis used to synthesize $AgNb_7O_{18}$ and $AgNb_{13}O_{33}$ [16,33], the current synthesis method does not involve the use of ethylene glycol ($(CH_2OH)_2$) as a complexing agent. Hence, both the undoped and dual-doped photocatalysts were fabricated, characterized, and tested to determine the influence of dual doping of Zr and La on the silver niobate towards better photocatalytic performance by degrading MB and RhB dyes.

2. Methodology

2.1. Chemicals used

Both niobium(V) chloride, $NbCl_5$ (99%), and silver nitrate, $AgNO_3$ (≥99.0%) were purchased from Sigma Aldrich. Zirconium nitrate, $Zr(NO_3)_4$The dyes, and lanthanum nitrate hexahydrate, $La(NO_3)_3{\cdot}6H_2O$ (≥96.0%) used for dual doping were purchased from BDH and Merck, respectively. Citric acid monohydrate (99.5%–100.5%) and absolute ethanol (≥99.9%) were also bought from Merck. The dyes used in the photocatalytic degradation experiment were methylene blue (MB, 85%, Merck) and Rhodamine B (RhB, ≥ 96.0%, Sigma Aldrich). A water purifier (Bibby Aquatron A4000D) was the source of the distilled H_2O used in the experiment.

2.2. Fabrication of photocatalysts

The sol-gel method used in the fabrication of silver niobate (undoped SN) was assisted by citric acid [34, 35]. The metal precursors included an equimolar ratio of $NbCl_5$ and $AgNO_3$. These were dissolved separately in absolute alcohol and distilled water, respectively. Citric acid monohydrate was then added to both solutions as a chelating agent. The molar ratio of $AgNO_3$, $NbCl_5$, and citric acid was 1:1:4. After 10 min of stirring, the two transparent liquids were mixed together. A white precipitate was observed upon mixing for 30 min. The evaporation of the product took place on a hot plate at 80 °C. After that, the crucible was used to contain the dried precursor and was heated at 800 °C for 5 h in a muffle furnace. It was left to cool overnight after the calcination process. All the content inside the crucible was ground into powder for weighing.

The 1%, 5%, and 10% Zr, La-dual doped SN were also synthesized the same way as above. The doping process for the synthesis involved replacing a certain amount of $NbCl_5$ and $AgNO_3$ with $Zr(NO_3)_4$ and $La(NO_3)_3{\cdot}6H_2O$, respectively, prior to mixing the two solutions. These samples were synthesized with the expectation that the La^{3+} cations would replace the Ag^{+} cations and the Zr^{4+} cations would replace the Nb^{5+} cations as shown in the literature [36, 37]. In this case, 1% Zr, La-dual doped SN corresponds to 1% La, 1% Zr, 99% Ag and 99% Nb, and so on.

2.3. Characterisation

X-ray diffraction (XRD) analysis was carried out on the fabricated photocatalysts. The powder X-ray diffractometer (Rigaku MiniFlex) was set to scan at a step rate of 5° min^{-1} within the 2θ range from 20° to 80°. The X-ray used is monochromatic CuKα radiation noted to have a wavelength of 1.5406 Å. Fourier transform infrared (FT-IR) spectroscopy was also carried out using Shimadzu IR Prestige-21 spectrometer and the transmittance data within the wavenumber range from 400 cm^{-1} to 4000 cm^{-1} were collected. Carbon-coated samples were prepared for field emission scanning electron microscopy (FE-SEM), where a scanning electron microscope (Tescan Lyra-3 Dual Beam instrument) was equipped with an energy dispersion spectrometer (Oxford Instruments) was used for observation and recording SEM images. During the FE-SEM session, Energy-dispersive X-ray (EDX) spectroscopy and mapping were also performed to determine the elemental composition of each sample. The UV-Vis diffuse reflectance spectroscopy (UV-Vis DRS) in absorption mode was carried out via UV-Vis-NIR Spectrophotometer Win Cary 5000. The absorbance spectra of the samples were recorded over the wavelength range of 200 nm–800 nm. Photoluminescence (PL) spectroscopy was another type of optical analysis carried out in this work. The instrument used was Jasco FP-8500ST and the excitation wavelength selected for this analysis was 266 nm. The emission spectra were recorded over the wavelength range of 360 nm–650 nm. An ultraviolet-visible spectrophotometer (Shimadzu UV-1900) was used for photocatalytic degradation measurements. The percentage degradation and rate constants were calculated using Eqs. (1) and (2) as shown below:

$$\%\ \text{Degradation} = \frac{C_0 - C}{C_0} \times 100\% \quad (1)$$

$$\ln(C / C_0) = -\text{kt} \quad (2)$$

2.4. Photocatalytic dye degradation

The photocatalytic performance of the fabricated photocatalysts was tested through MB and RhB dye degradation in aqueous solutions. In the experiment, 50 mL of aqueous MB and RhB solutions (10 mg L^{-1}) were transferred into the reaction vessels and the amount of photocatalyst added was 20 mg. The solid particles in these mixtures were dispersed via 5 min of sonication. The reaction vessels were placed in a TOPT-V photochemical reactor equipped with a 300 W xenon long-arc lamp. For the first 30 min in the dark, the adsorption and desorption of dye molecules on the surface of photocatalysts were allowed to reach equilibrium. The vessels were irradiated with visible light for 5 h and in between each hour of irradiation, 3 mL of aliquots were withdrawn and centrifuged. The concentration of the dyes after centrifuging was monitored using a UV-Vis spectrophotometer.

3. Results and discussions

3.1. X-ray diffraction

XRD analysis was used to identify the crystal structure of undoped SN, 1%, 5%, and 10% Zr, La-dual doped SN. The XRD patterns are shown in Figure 1. The XRD patterns of the undoped SN and Zr, La-dual doped SN were compared with that of the XRD standards to confirm their crystal structure. With reference to the diffraction patterns (114), (220), (028), and (228) seen in the $AgNbO_3$ (No: 01-078-2584) standard are the corresponding planes for 32.25°, 46.07°, 57.49°, and 67.48° 2θ values. These values are found in all four synthesized samples [38]. This confirmed that $AgNbO_3$ has been successfully synthesized. In the XRD pattern of undoped SN, additional peaks that belong to $AgNb_3O_8$ (No: 01-077-4048) were also observed [39]. Some peaks corresponding to $AgNb_3O_8$ present in undoped SN are the (211) (040), (140), (221), and (311) reflections, which were observed at 2θ values of 27.91°, 29.04°, 29.75°, 30.45°, and 32.29°. Hence, undoped SN contains both $AgNbO_3$ and $AgNb_3O_8$ phases.

The XRD patterns of undoped SN show that the material consists of two silver niobate phases. When the Zr, La-dual doping percentage of the silver niobate sample increased to 1% and 5%, the diffraction peaks which correspond to $AgNb_3O_8$ decreased in intensity while $AgNbO_3$ peaks became more prominent. In the case of 10% Zr, La-dual doped SN, peaks corresponding to $AgNb_3O_8$ had almost completely disappeared and may indicate that it consists of mainly the $AgNbO_3$ phase. This suggests that dual doping has somehow favoured the formation of $AgNbO_3$ over $AgNb_3O_8$. The changes in the XRD patterns also indicate that the dual doping of Zr and La has an impact on the crystal structure of the silver niobate. From the XRD data, the crystallite size (D) was calculated and found to be between 33.88 and 44.02 nm using the Scherrer equation [40]. Similarly, lattice parameters and cell volume were also calculated and shown in Table 1. Calculation of the crystallite size was done using Eq. (3), the Scherrer equation as shown below:

$$D = \frac{k\lambda}{\beta\cos\theta} \quad (3)$$

where D represents crystallite size in nanometres, k represents Scherrer constant and is assumed to be 0.9 in this study, λ represents X-ray wavelength which was measured to be 1.5406 Å, β represents FWHM value in radians of a selected peak, and θ represents Bragg angle.

The plots in Figure 2 show the changes in the lattice parameters with respect to the percentage of Zr, La-dual doping. The values of the lattice parameters '*a*' and '*c*' in Figure 2 (i) are increasing while '*b*' in Figure 2(ii) is decreasing. Furthermore, there is a slight increase in the unit cell volume as shown in Figure 2(ii) from undoped SN (483.73 $Å^3$) to 10% Zr, La-dual doped SN (485.81 $Å^3$). The changes seen in the lattice parameters suggested that Zr and La are influencing the crystal structure and have been successfully doped into the silver niobate structure. Moreover, the expanded unit cell may be the result of the larger Zr^{4+} (0.72 Å) and La^{3+} (1.36 Å) cations substituting the smaller Nb^{5+} (0.64 Å) and Ag^{+} (1.28 Å) cations in the structure [41].

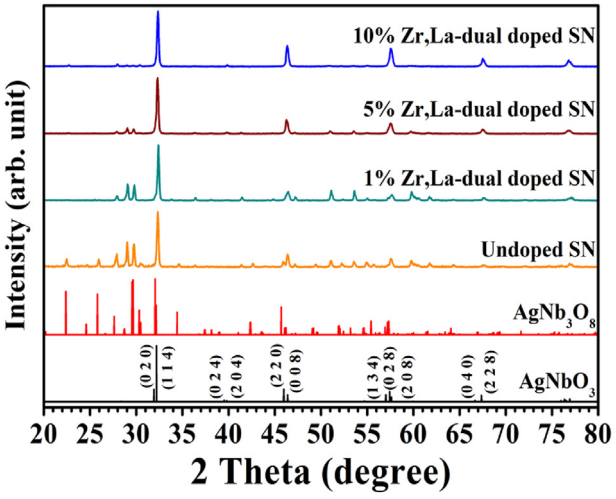

Figure 1. XRD patterns of the fabricated photocatalysts.

3.2. Fourier transform infrared spectroscopy

Figure 3 shows the FT-IR spectra of undoped SN, 1%, 5%, and 10% Zr, La-dual doped SN. A broad band was seen within the 400-1000 cm^{-1} region and was labeled as ν(Nb–O). A similar intense band had also been reported in the literature for hydrothermally-synthesized $AgNbO_3$ and is related to the vibration of Nb–O bonds [42]. However, the band exhibited by the synthesized silver niobate and Zr, La-dual doped silver niobates were further split into about five smaller shoulder peaks designated at around 500 cm^{-1}, 570 cm^{-1}, 650 cm^{-1}, 720 cm^{-1}, and 860 cm^{-1} as shown in Table 2 [43]. The FT-IR spectra of undoped $AgNbO_3$ reported by Yang *et al.* did not show such characteristic splitting of the ν(Nb–O) band [42]. Since the XRD had shown that both $AgNbO_3$ and $AgNb_3O_8$ phases are present in the photocatalysts, it is likely that the observed splitting is a result of the $AgNb_3O_8$ phase. With reference to the literature, corner-sharing NbO_6 octahedra are responsible for the peaks at 570 cm^{-1}, 650 cm^{-1}, and 720 cm^{-1} [43]. Edge-sharing NbO_6 octahedra, on the other hand, was assigned at 500 cm^{-1} and 860 cm^{-1} [43]. Furthermore, the splitting seen in the ν(Nb–O) band becomes less prominent as Zr and La dual doping intensifies. This suggests that the $AgNbO_3$ phase has increased with the dual doping as indicated by the XRD patterns.

Other metal oxide bands such as those of Ag–O (~700 cm^{-1}) [42], Zr–O (~500 cm^{-1}) [44], and La–O (~510 cm^{-1} and 648 cm^{-1}) [45], may also be present within the region of ν(Nb–O) but are overlapped due to the close proximity of these metal oxide bands with ν(Nb–O). It is also possible that the small amount of Zr and La present might make it difficult to be detected by the FT-IR spectrometer.

Table 1. The average crystallite size (D), lattice parameters '*a*', '*b*', '*c*' and cell volume of the photocatalysts.

Sample	D (nm)	Lattice parameters			V ($Å^3$)
		'*a*' (Å)	'*b*' (Å)	'*c*' (Å)	
SN	44.02 ± 3.27	5.5440	5.5700	15.6650	483.7365
1% Zr, La dual-doped SN	35.48 ± 15.11	5.5420	5.5900	15.6610	485.1743
5% Zr,La-dual doped SN	33.88 ± 13.03	5.5400	5.5680	15.7070	484.5094
10% Zr,La-dual doped SN	35.06 ± 7.94	5.5507	5.5750	15.6990	485.8080

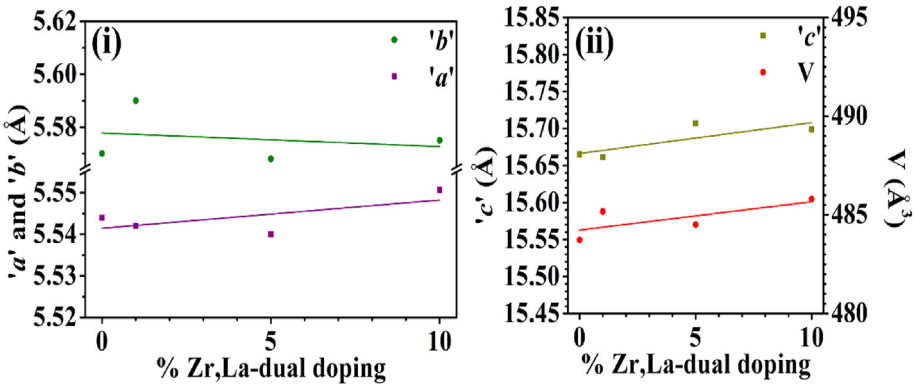

Figure 2. Lattice parameters **(i)** '*a*', '*b*', and **(ii)** '*c*' and cell volume, V, of the photocatalysts.

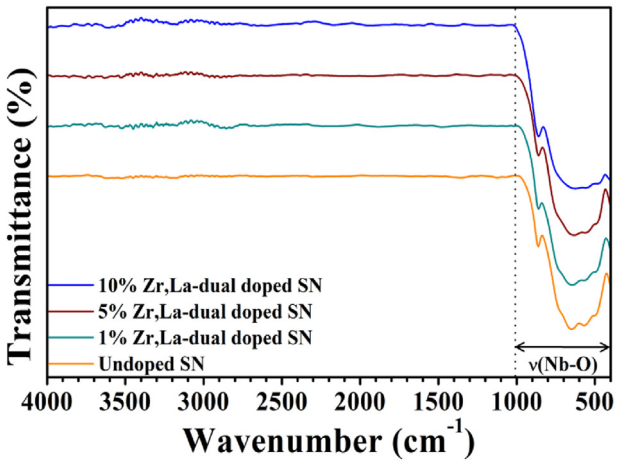

Figure 3. FT-IR spectra of the photocatalysts.

Table 2. Reported and observed FT-IR stretching frequencies with respect to the type of NbO_6 octahedra [43].

Type of NbO_6 octahedra	Reported stretching frequencies in literature (cm^{-1})	Observed stretching frequencies in this work (cm^{-1})
Corner-sharing	580	570
	620	650
	700	720
Edge-sharing	500	500
	850	860

Referring back to the FT-IR spectra of the samples, no peaks located at approximately 1384 cm^{-1} were observed [46]. This indicates the absence of the NO_3^- group in the samples and that the metal nitrate precursors have been successfully converted into oxides. In addition to this, the samples were free of citric acid used in the synthesis as a chelating agent. This was ascertained because the spectra did not show the presence of 3139 cm^{-1} and 1612 cm^{-1} peaks which corresponds to O–H and COO^- functional groups, respectively [46].

3.3. Field emission scanning electron microscopy

The FE-SEM and EDX analysis has been used to capture images of undoped SN, 1%, 5%, and 10% Zr, La-dual doped SN as shown in Figure 4. In terms of morphology, there were changes seen as the silver niobate was doped with an increased percentage of Zr and La. The undoped SN particles were large (1.21 μm) microstructures with a prism-like appearance. The particles of 1%, 5%, and 10% Zr, La-dual doped SN were comparatively smaller (0.60 μm, 0.54 μm, and 0.57 μm) than those measured from undoped SN. The average particle size of undoped SN and Zr, La-dual doped SNs were smaller than that of $AgNbO_3$ fabricated via solid state synthesis [29]. Furthermore, the morphology of the particles in undoped SN was distinctly different from those in Zr, La-dual doped samples. This may be due to the structural change from a mixture of $AgNbO_3$ and $AgNb_3O_8$ to single-phase $AgNbO_3$ as observed in the XRD results.

The presence of Ag, Nb, La, and Zr in 10% Zr, La-dual doped SN was mapped by the EDX analysis as displayed in Figures 4(e)–(i). The EDX mappings show that the elements are uniformly distributed throughout the samples. The number of coloured spots in La and Zr is smaller than that of Ag and Nb. This is expected as the former pair of elements are the dopants and are present in only small quantities.

3.4. Optical studies

In order to explore the optical properties of the fabricated photocatalysts, PL analysis was carried out. The results are shown as the emission spectra in Figure 5. Overall, the undoped SN showed higher PL intensity as compared to the dual doped samples. This may indicate that the charge carriers generated by all three dual-doped photocatalysts are less prone to recombine than the silver niobate [47]. As the concentration of the dual dopants was increased from 1% to 10%, the PL intensity also increased. The likely reason for this may be due to the increasing quantity of photo-generated electron-hole pairs with an increasing percentage of dual doping. In turn, more electrons and holes were recombined to yield a higher recombination rate, and the PL intensity of 10% Zr, La-dual doped SN was perceived as the highest among the three Zr, La-dual doped silver niobates [48]. Further observation of the PL spectra showed that the highest peak shifted with an increasing percentage of the dual dopants. As the different materials may produce different PL spectra, this shifting may be due to the transition from $AgNbO_3$/$AgNb_3O_8$ mixture to pure $AgNbO_3$, as indicated by XRD and FT-IR.

In Figure 6(a), band tailing had been observed in the absorbance spectra of undoped SN and is distinctive from the spectra of the dual doped photocatalysts. The presence of the band tailing observed may be due to the high amount of $AgNb_3O_8$ phase present in undoped SN as compared to other samples. Using the Tauc plots derived from the UV-Vis absorption spectra, the band gap values of the fabricated photocatalysts were determined as shown in Figure 6(b), respectively. The estimated band gap energy for undoped SN was 2.96 eV, whereas the three dual-doped photocatalysts showed a value of 2.89 eV. The sudden change in band gap energies may be associated with intermediate states introduced by La^{3+} and Zr^{4+} which had been doped into the SN. The lower band gap energies of the dual doped samples indicate that they are more responsive to visible light than undoped SN. However, increasing the dual doping percentage of La and Zr from 1% to 10% did not further influence the band gap to change. Eq. (4) below was used to produce the Tauc plots:

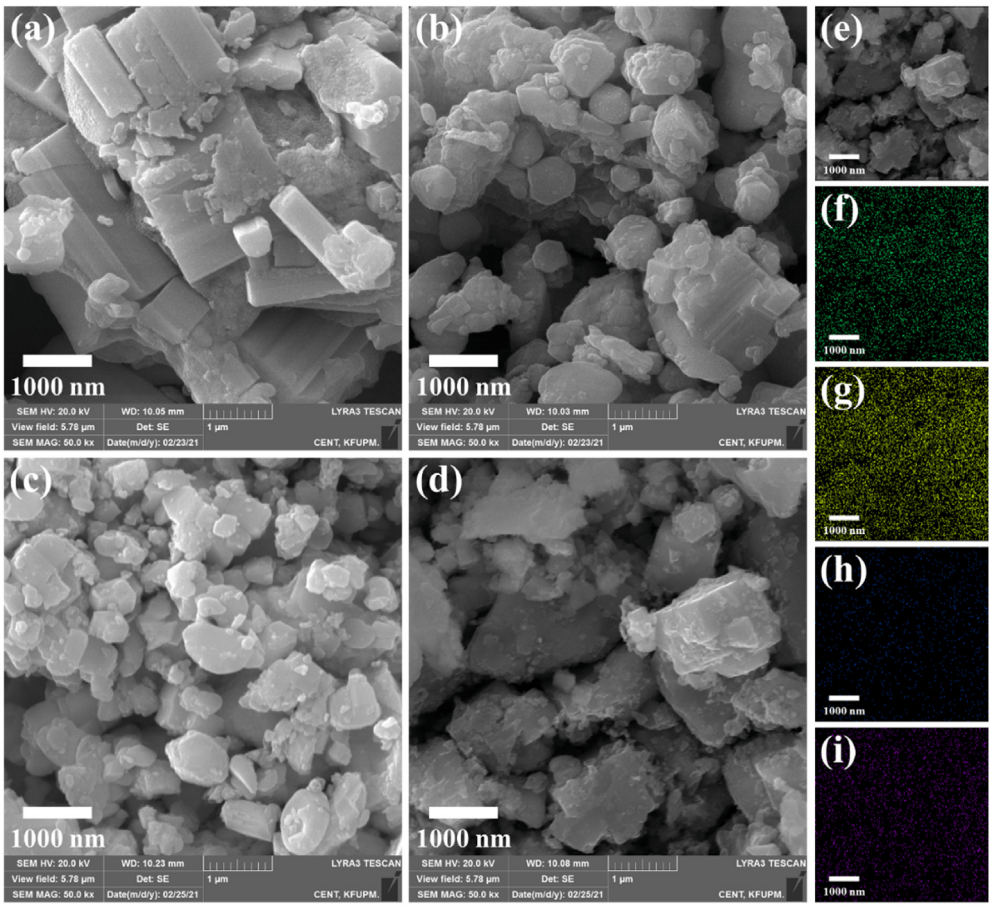

Figure 4. SEM images of (a) undoped SN, (b) 1%, (c) 5%, and (d) 10% Zr, La-dual doped SN, together with the EDX mappings of (e) 10% Zr, La-dual doped SN, showing (f) Ag, (g) Nb, (h) La, and (i) Zr.

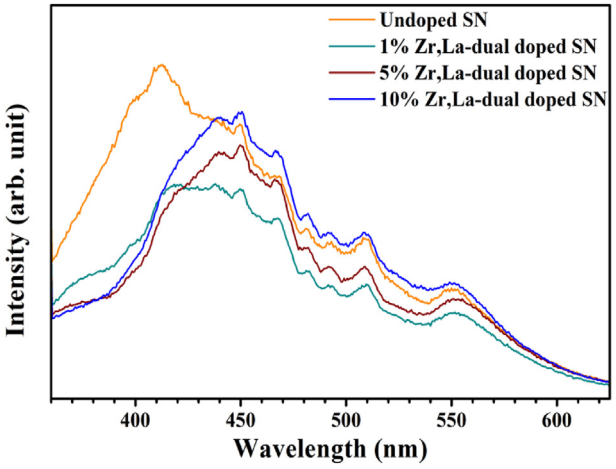

Figure 5. PL spectra of the photocatalysts.

$$(\alpha h\nu)^n = k(h\nu - E_g) \quad (4)$$

where α represents optical absorption coefficient, h represents Planck constant, ν represents the frequency of light, n represents an index for optical transition type and is assumed to be 2, k represents band-tailing constant but is ignored in this study, and E_g represents band gap energy.

3.5. Photocatalytic performance of MB and RhB

The fabricated photocatalysts were used in the dye degradation experiments. The results of MB dye degradation were also visually represented using the $-\ln(C/C_0)$ against time plots and the percentage degradation graphs as seen in Figure 7(a) and (b), respectively. The photocatalytic degradation performance was evaluated using the plots in Figure 7(a) [49]. The figure represents the MB dye photocatalytic degradation by the photocatalysts. The control experiment in the same figure shows that photolysis has a negligible contribution to the breaking down of MB dyes as its rate constant reached only 0.00016 min^{-1} at the end of the experiment. The calculated rate constants of undoped SN, 1%, 5% and 10% Zr, La-dual doped SN are 0.00366 min^{-1}, 0.00485 min^{-1}, 0.00396 min^{-1}, and 0.00455 min^{-1}, respectively. The lowest rate constant is shown by undoped SN for MB photocatalytic degradation. On the other hand, the highest photocatalytic degradation was achieved by 1% Zr, La-dual doped SN. Dual-doping the silver niobate with 5% Zr and La resulted in a lower rate constant. Figure 7(b) shows the percentage of MB dye degraded after 5 h by the samples. Undoped SN, 1%, 5% and 10% Zr, La-dual doped SN have the percentage photocatalytic degradation of 67.9%, 77.3%, 70.6% and 75.9%, respectively. The plot also shows that 1% Zr, La-dual doped SN is the best in degrading MB dye. Overall, the dual-doped photocatalysts are better at degrading MB dye than undoped SN. The improvement by codoping La and Zr into metal oxide was also reported in the literature, where the degradation of MB using La, Zr-codoped ZnO was higher than that of undoped ZnO [50]. When 5% Zr, La-dual doped SN was used in the photocatalytic degradation of MB, its performance was lower than that of 1% and 10% Zr, La-dual doped SNs. This is likely due to the change in phase composition with increasing dual doping percentage as seen in the XRD diffraction patterns of the samples (Figure 1).

Figure 8(a) shows the $-\ln(C/C_0)$ against time plots of RhB dye degraded by the fabricated photocatalysts. The sample with the lowest

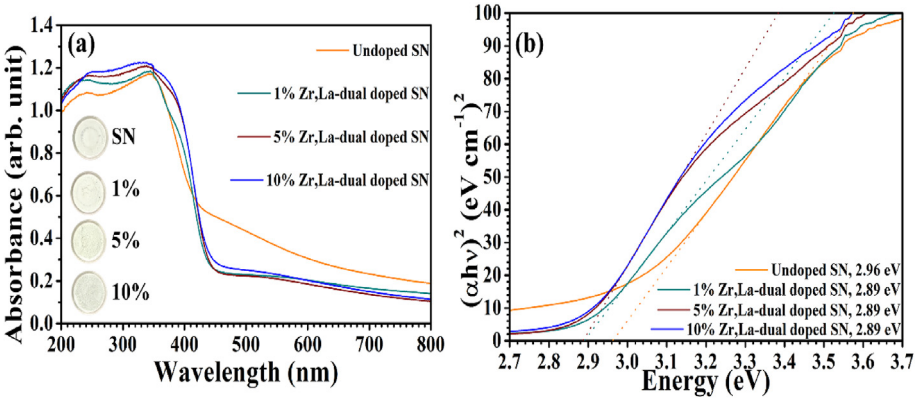

Figure 6. (a) UV-Vis absorption spectra (with inset showing the colours of the samples) and (b) Tauc plots of the photocatalysts.

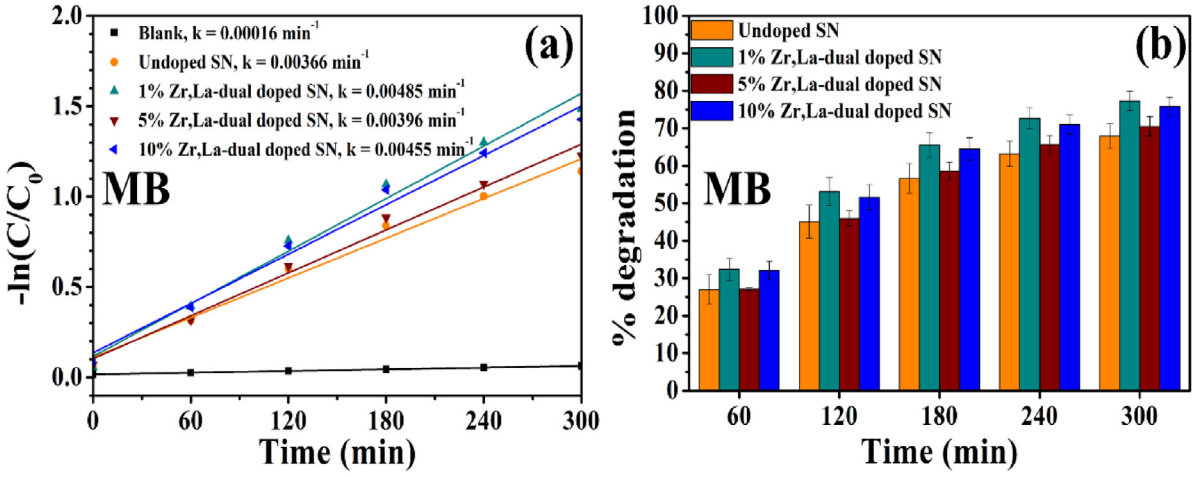

Figure 7. (a) Rate constants and (b) photocatalytic degradation efficiency of the photocatalysts in degrading MB.

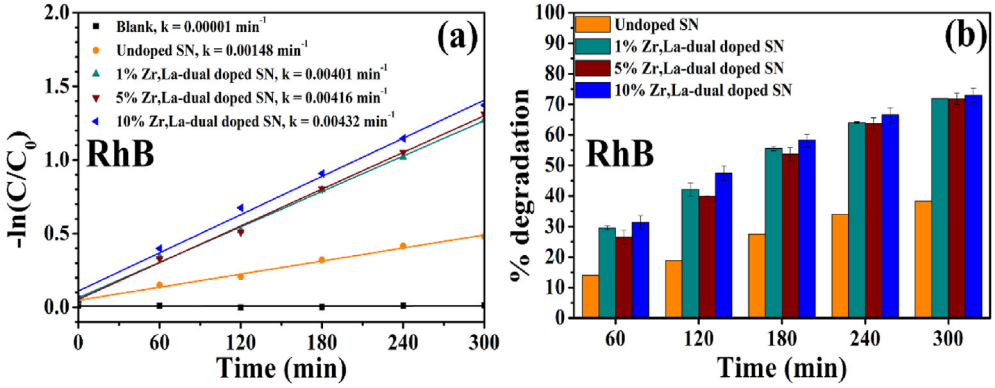

Figure 8. (a) Rate constants and (b) photocatalytic degradation efficiency of the photocatalysts in degrading RhB.

rate constant is undoped SN (0.00148 min^{-1}), followed by 1% Zr, La-dual doped SN (0.00401 min^{-1}), 5% Zr, La-dual doped SN (0.00416 min^{-1}). Finally, the fastest reaction was achieved by 10% Zr, La-dual doped SN at the rate constant of 0.00432 min^{-1}. It was also shown that the photolysis of RhB is negligible, with a rate constant of only 0.00001 min^{-1}. The improvement produced by the dual doping is very significant and the rate constants of these dual doped samples are more than twice that of undoped SN. With reference to the estimated band gap energies, it is likely that the improvement is due to the ability of the dual-doped samples to utilize light with a longer wavelength. The percentage of RhB dye degraded by each of the samples after 5 h is shown in Figure 8(b). The performance of undoped SN, 1%, 5%, and 10% Zr, La-dual doped SN were determined to be 38.2%, 71.9%, 71.7%, and 73.0%, respectively. These plots show that 10% Zr, La-dual doped SN is not only the fastest to undergo photocatalytic dye degradation but also degraded the highest amount of RhB. It was noted that the rate constant in which RhB was degraded is lower than that of MB. This is because RhB and MB interact differently with the photocatalyst which may cause the dye molecules to be degraded at different rates [51]. Similar to MB degradation, fluctuation is also observed in RhB percentage photocatalytic degradation results and may also be connected to the change in phase composition among the samples [52].

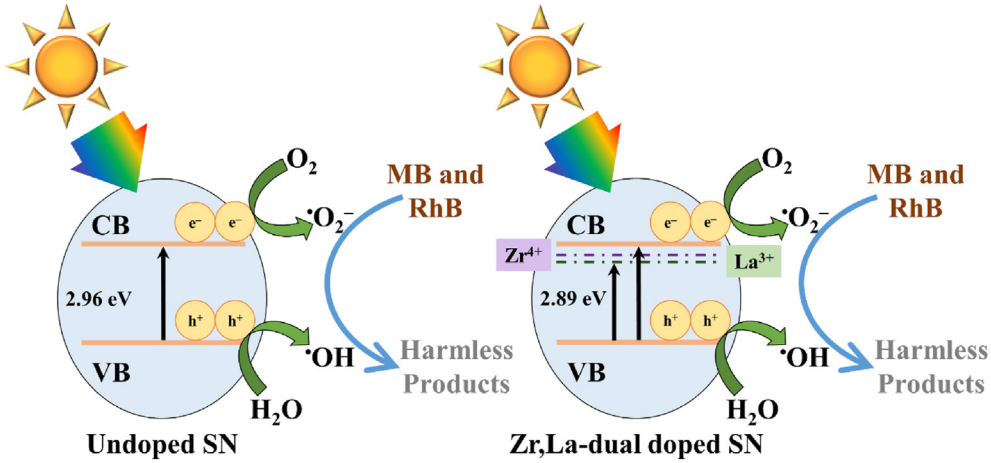

Figure 9. Proposed mechanism of dye degradation exhibited by undoped SN, and Zr, La-dual doped SN.

3.6. The mechanism for photocatalytic dye degradation

Figure 9 shows the proposed photocatalytic dye degradation mechanism of undoped SN and Zr, La-dual doped SN photocatalysts. As indicated by the UV-Vis DRS analysis, the band gap energy of silver niobate decreased when it was dual doped with 1% Zr, La. When the dual doping increased further to 10%, the band gap remained the same. All Zr, La-dual doped silver SNs have smaller band gap energy when compared with that of undoped SN due to the formation of Zr^{4+} and La^{3+} intermediate states below the conduction band [53, 54]. These intermediate states allow visible light of longer wavelengths to be absorbed by the photocatalysts. In general, it is shown that the photocatalytic degradation of MB and RhB dyes by the silver niobate had been enhanced through dual doping. One possible explanation for this is the reduced particle size after Zr, La-dual doping as observed in FE-SEM analysis. The reduced particle size of the photocatalyst increases the surface area-to-volume ratio and hence, improves the photocatalytic degradation of the dyes. Based on the results of the XRD analysis, another reason for the improvement could be due to the transition of $AgNbO_3$/$AgNb_3O_8$ to $AgNbO_3$-rich phase as the Zr, La dual doping percentage increases.

It was experimentally shown in the literature that $AgNbO_3$ can decompose dyes using at least three types of species; photogenerated h^+, $^{\cdot}OH$, and $^{\cdot}O_2^-$ free radicals [55]. The valence band (+2.8 eV) and conduction band edges (−0.1 eV) of $AgNbO_3$ [55], are in the appropriate positions to carry out the redox reactions ($^{\cdot}OH/OH^-$ = −0.046 V [56], and $^{\cdot}OH/H_2O$ = +2.32 V [57], respectively) for the generation of these species.

4. Conclusion

In conclusion, the silver niobate photocatalysts were synthesized via the sol-gel method. XRD analysis shows that undoped SN contains both $AgNbO_3$ and $AgNb_3O_8$ phases. The amount of $AgNb_3O_8$ phases decreases with increasing Zr and La-dual doping. This transition was also detected in FT-IR analysis where the peaks of NbO_6 octahedra change in intensity with different percentages of Zr, La-dual doping. The presence of $AgNbO_3$ and $AgNb_3O_8$ caused the particles in undoped SN to appear prism-like with an average particle size of 1.21 μm, as seen in the FESEM images. The average particle sizes are smaller in the dual doped samples (0.54–0.60 μm) and are more agglomerated than undoped SN. Nb, Ag, Zr, and La are present in 10% Zr, La-dual doped SN, as indicated by the EDX mapping. Overall, all the dual doped SNs have a lower electron-hole recombination rate and band gap energy than undoped SN. As indicated by the photocatalytic dye degradation experiments, it is revealed that the Zr, La-dual doped samples performed better than undoped SN. The change in composition between the two silver niobate phases may also play a part in the enhancements of photocatalysis. Therefore, dual-doping of silver niobate by Zr, La is a useful strategy for enhancing its photocatalytic activities.

Declarations

Author contribution statement

Chun Mun Khor: Performed the experiments; Analyzed and interpreted the data; Wrote the paper.

Mohammad Mansoob Khan, Mohammad Hilni Harunsani: Conceived and designed the experiments; Analyzed and interpreted the data; Contributed reagents, materials, analysis tools or data.

Abuzar Khan, Mohd Yusuf Khan: Analyzed and interpreted the data; Contributed reagents, materials, analysis tools or data.

Funding statement

This work was supported by Universiti Brunei Darussalam (UBD/RSCH/1.4/FICBF(b)/2021/035).

Data availability statement

Data will be made available on request.

Declaration of interests statement

The authors declare no conflict of interest.

Additional information

The authors declare no conflict of interest.

Acknowledgements

Abuzar Khan and Mohd Yusuf Khan acknowledge the Interdisciplinary Research Center for Hydrogen and Energy Storage, King Fahd University of Petroleum & Minerals (KFUPM), Dhahran, 31261, Saudi Arabia for the research support.

References

[1] K. Zhang, Y. Lin, Z. Muhammad, C. Wu, S. Yang, Q. He, X. Zheng, S. Chen, B. Ge, L. Song, Active {010} facet-exposed Cu_2MoS_4 nanotube as high-efficiency photocatalyst, Nano Res. 10 (11) (2017) 3817–3825.

[2] A. Ghosh, C.S. Kavitha, R.S. Keri, Fe_3O_4@cysteine nanocomposite: an efficient and reusable catalyst for the facile, green, one-pot synthesis of 1,4-dihydropyridine via Hantzsch reaction, Chem. Data Collect. 33 (2021) 1–13.

[3] L. Jiang, J. Yang, S. Zhou, H. Yu, J. Liang, W. Chu, H. Li, H. Wang, Z. Wu, X. Yuan, Strategies to extend near-infrared light harvest of polymer carbon nitride photocatalysts, Coord. Chem. Rev. 439 (2021) 1–20.

[4] P. Sarkar, S.A. Moyez, A. Dey, S. Roy, S.K.K. Das, Experimental investigation of photocatalytic and photovoltaic activity of titania/rice husk crystalline nano-silica hybrid composite, Sol. Energy Mater. Sol. Cells 172 (2017) 93–98.

[5] M.M. Khan, D. Pradhan, Y. Sohn, in: M.M. Khan, D. Pradhan, Y. Sohn (Eds.), Nanocomposites for visible light-induced photocatalysis, 1st ed., Springer International Publishing, 2017.

[6] M.M. Khan, S.A. Ansari, D. Pradhan, M.O. Ansari, D.H. Han, J. Lee, M.H. Cho, Band gap engineered TiO_2 nanoparticles for visible light induced photoelectrochemical and photocatalytic studies, J. Mater. Chem. A 2 (3) (2014) 637–644.

[7] J. Xue, T. Chen, Y. Meng, X. Zhou, G. Pan, Z. Ni, S. Xia, Efficient detoxication of heterocyclics by layered double hydroxides contained different cobalt components as photocatalysts based on controllable application of active free radicals, J. Photochem. Photobiol. A Chem. 371 (2019) 33–43.

[8] M.M. Khan, in: Khan, M.M (Ed.), Chalcogenide-based nanomaterials as photocatalysts, 1st ed., Elsevier, 2021.

[9] Y. Ye, H. Yang, X. Wang, W. Feng, Photocatalytic, fenton and photo-fenton degradation of RhB over Z-scheme g-C_3N_4/$LaFeO_3$ heterojunction photocatalysts, Mater. Sci. Semicond. Process 82 (2018) 14–24.

[10] M.M. Khan, S.F. Adil, A. Al-Mayouf, Metal oxides as photocatalysts, J. Saudi Chem. Soc. 19 (5) (2015) 462–464.

[11] A.B. Djurišić, Y. He, A.M.C. Ng, Visible-light photocatalysts: prospects and challenges, APL Mater. 8 (3) (2020) 1–24.

[12] S.K. Loeb, P.J.J. Alvarez, J.A. Brame, E.L. Cates, W. Choi, J. Crittenden, D.D. Dionysiou, Q. Li, G. Li-Puma, X. Quan, D.L. Sedlak, T. David Waite, P. Westerhoff, J.H. Kim, The technology horizon for photocatalytic water treatment: sunrise or sunset? Environ. Sci. Technol. 53 (6) (2019) 2937–2947.

[13] E.L. Cates, Photocatalytic water treatment: so where are we going with this? Environ. Sci. Technol. 51 (2) (2017) 757–758.

[14] A. Kania, Anisotropic dielectric properties of $AgNbO_3$ single crystals, Ferroelectrics 404 (1) (2010) 152–156.

[15] Y. Qian, J. Wang, S.U. Asif, J. Xie, W. Hu, Origins of dielectric relaxations in $AgNb_7O_{18}$ ceramic, Ceram. Int. 46 (14) (2020) 23021–23026.

[16] X.X. Liu, C. Qin, L. Cao, Y. Feng, Y. Huang, L. Qin, H.J. Seo, A silver niobate photocatalyst $AgNb_7O_{18}$ with perovskite-like structure, J. Alloys Compd. 724 (2017) 381–388.

[17] C. Wang, J. Yan, X. Wu, Y. Song, G. Cai, H. Xu, J. Zhu, H. Li, Synthesis and characterization of AgBr/$AgNbO_3$ composite with enhanced visible-light photocatalytic activity, Appl. Surf. Sci. 273 (2013) 159–166.

[18] X. Kong, Z. Guo, Q. Lu, J. Huang, L. Cao, L. Yin, J. Li, Q. Feng, Platelike $Ag_2Nb_4O_{11}$ mesocrystals: soft chemical synthesis, formation mechanism and enhanced photocatalytic performance, J. Alloys Compd. 686 (2016) 48–54.

[19] C.M. Khor, M.M. Khan, A. Khan, M.Y. Khan, M.H. Harunsani, La-substituted $AgNbO_3$ for photocatalytic degradation of rhodamine B and methylene blue dyes, React. Kinet. Mech. Catal. (2022).

[20] Z. Yu, B. Zhan, B. Ge, Y. Zhu, Y. Dai, G. Zhou, F. Yu, P. Wang, B. Huang, J. Zhan, Synthesis of high efficient and stable plasmonic photocatalyst Ag/$AgNbO_3$ with specific exposed crystal-facets and intimate heterogeneous interface via combustion route, Appl. Surf. Sci. 488 (2019) 485–493.

[21] K. Han, N. Luo, Y. Jing, X. Wang, B. Peng, L. Liu, C. Hu, H. Zhou, Y. Wei, X. Chen, Q. Feng, Structure and energy storage performance of Ba-modified AgNbO3 lead-free antiferroelectric ceramics, Ceram. Int. 45 (5) (2019) 5559–5565.

[22] G. Li, S. Yan, Z. Wang, X. Wang, Z. Li, J. Ye, Z. Zou, Synthesis and visible light photocatalytic property of polyhedron-shaped $AgNbO_3$, J. Chem. Soc. Dalt. Trans. 3 (40) (2009) 8519–8524.

[23] J.W. Liu, G. Chen, Z.H. Li, Z.G. Zhang, Hydrothermal synthesis and photocatalytic properties of $ATaO_3$ and $ANbO_3$ (A = Na and K), Int. J. Hydrogen Energy 32 (13) (2007) 2269–2272.

[24] J.M. Coronado, F. Fresno, M.D. Hernández-Alonso, R. Portela, in: J.M. Coronado, F. Fresno, M.D. Hernández-Alonso, R. Portela (Eds.), Design of advanced photocatalytic materials for energy and environmental applications, Springer, London, 2013.

[25] J. Gao, Q. Liu, J. Dong, X. Wang, S. Zhang, J.F. Li, Local structure heterogeneity in Sm-doped $AgNbO_3$ for improved energy-storage performance, ACS Appl. Mater. Interfaces 12 (5) (2020) 6097–6104.

[26] P. Shi, X. Wang, X. Lou, C. Zhou, Q. Liu, L. He, S. Yang, X. Zhang, Significantly enhanced energy storage properties of Nd^{3+} doped $AgNbO_3$ lead-free antiferroelectric ceramics, J. Alloys Compd. 877 (2021) 1–9.

[27] U. Farid, A.S. Gibbs, B.J. Kennedy, Impact of Li doping on the structure and phase stability in $AgNbO_3$, Inorg. Chem. 59 (17) (2020) 12595–12607.

[28] R. Muduli, R. Pattanayak, S. Kumar, S.K. Kar, P. Kumar, S. Panigrahi, R.K. Panda, Dielectric, ferroelectric and impedance spectroscopic study of Ta_2O_5, Sb_2O_5, and V_2O_5-doped $AgNbO_3$ ceramic, J. Alloys Compd. 656 (2016) 33–44.

[29] C. Xu, Z. Fu, Z. Liu, L. Wang, S. Yan, X. Chen, F. Cao, X. Dong, G. Wang, La/Mn codoped $AgNbO_3$ lead-free antiferroelectric ceramics with large energy density and power density, ACS Sustain. Chem. Eng. 6 (12) (2018) 16151–16159.

[30] W. Chao, T. Yang, Y. Li, Z. Liu, Enhanced energy storage density in Ca and Ta co-doped $AgNbO_3$ antiferroelectric ceramics, J. Am. Ceram. Soc. 103 (12) (2020) 7283–7290.

[31] K. Han, N. Luo, S. Mao, F. Zhuo, L. Liu, B. Peng, X. Chen, C. Hu, H. Zhou, Y. Wei, Ultrahigh energy-storage density in A-/B-site co-doped $AgNbO_3$ lead-free antiferroelectric ceramics: insight into the origin of antiferroelectricity, J. Mater. Chem. A 7 (46) (2019) 26293–26301.

[32] W. Liu, H. Wang, $AgNbO_3$ ceramics synthesized by aqueous solution-gel method, J. Sol-Gel Sci. Technol. 58 (1) (2011) 96–101.

[33] X. Liu, C. Qin, Y. Huang, L. Qin, H.J. Seo, A new silver niobate photocatalyst $AgNb_{13}O_{33}$: synthesis, structure and photochemical properties, J. Taiwan Inst. Chem. Eng. 78 (2017) 530–538.

[34] C.M. Khor, M.M. Khan, A. Khan, M.Y. Khan, M.H. Harunsani, Zr-doped silver niobates for photocatalytic degradation of methylene blue and rhodamine B dyes, Optik (Stuttg) 267 (2022) 1–11.

[35] C.M. Khor, M.M. Khan, M.Y. Khan, A. Khan, M.H. Harunsani, Effect of La^{3+}-doping in silver niobate for enhanced photocatalytic degradation of methylene blue and rhodamine B, Chem. Phys. Impact 4 (May) (2022) 1–10.

[36] G. Li, T. Kako, D. Wang, J. Ye, Enhanced photocatalytic activity of La-doped $AgNbO_3$ under visible light irradiation, J. Chem. Soc. Dalt. Trans. 13 (2009) 2423–2427.

[37] X. Wang, P. Ren, D. Ren, L. Xie, T. Li, J. Xu, Y. Xi, C. Yang, B-site acceptor doped $AgNbO_3$ lead-free antiferroelectric ceramics: the role of dopant on microstructure and breakdown strength, Ceram. Int. 47 (3) (2021) 3699–3705.

[38] I. Levin, V. Krayzman, J.C. Woicik, J. Karapetrova, T. Proffen, M.G. Tucker, I.M. Reaney, Structural changes underlying the diffuse dielectric response in $AgNbO_3$, Phys. Rev. B - Condens. Matter Mater. Phys. 79 (10) (2009) 1–14.

[39] P. Rozier, O. Szajwaj, Crystal chemistry in the Ag_2O-Nb_2O_5 system. $AgNb_3O_8$ structure determination, J. Solid State Chem. 181 (2) (2008) 228–234.

[40] T.C. Bhagya, S.A. Rajan, S.M.A. Shibli, In situ tuning of band gap of Sn doped composite for sustained photocatalytic hydrogen generation under visible light irradiation, Int. J. Hydrogen Energy (2020) 1–13.

[41] R.D. Shannon, Revised effective ionic radii and systematic studies of interatomic distances in halides and chalcogenides, Acta Crystallogr. Sect. A 32 (5) (1976) 751–767.

[42] M. Yang, Y. Pu, W. Wang, J. Li, X. Guo, R. Shi, Y. Shi, Highly efficient Ag_2O/$AgNbO_3$ p-n heterojunction photocatalysts with enhanced visible-light responsive activity, J. Alloys Compd. 811 (2019) 1–11.

[43] M. Tatsumisago, A. Hamada, T. Minami, M. Tanaka, Infrared spectra of rapidly quenched glasses in the systems Li_2O-RO-Nb_2O_5 (R=Ba, Ca, Mg), J. Am. Ceram. Soc. 66 (2) (1983) 117–119.

[44] N.C. Horti, M.D. Kamatagi, S.K. Nataraj, M.N. Wari, S.R. Inamdar, Structural and optical properties of zirconium oxide (ZrO_2) nanoparticles: effect of calcination temperature, Nano Express 1 (1) (2020) 1–9.

[45] H. Kabir, S.H. Nandyala, M.M. Rahman, M.A. Kabir, A. Stamboulis, Influence of calcination on the sol–gel synthesis of lanthanum oxide nanoparticles, Appl. Phys. A Mater. Sci. Process 124 (12) (2018) 1–11.

[46] S.H. Xiao, W.F. Jiang, L.Y. Li, X.J. Li, Low-temperature auto-combustion synthesis and magnetic properties of cobalt ferrite nanopowder, Mater. Chem. Phys. 106 (1) (2007) 82–87.

[47] A.B. Ali Baig, V. Rathinam, J. Palaninathan, Fabrication of Zr-doped SnO_2 nanoparticles with synergistic influence for improved visible-light photocatalytic action and antibacterial performance, Appl. Water Sci. 10 (54) (2020) 1–12.

[48] Z. Wan, M. Hu, B. Hu, T. Yan, Vacancy induced photocatalytic activity of La doped $In(OH)_3$ for CO_2 reduction with water vapor, Catal. Sci. Technol. 10 (2020) 2893–2904.

[49] A. Kumar, G. Pandey, Photodegradation of methyl orange in aqueous solution by the visible light active Co:La:TiO_2 nanocomposite, Chem. Sci. J. 8 (3) (2017) 1–9.

[50] H.F. Moafi, M.A. Zanjanchi, A.F. Shojaie, Lanthanum and zirconium co-doped ZnO nanocomposites: synthesis, characterization and study of photocatalytic activity, J. Nanosci. Nanotechnol. 14 (9) (2014) 7139–7150.

[51] X. Ji, Y. Guo, S. Hua, H. Li, S. Zhang, Interaction-determined sensitization photodegradation of dye complexes by boron nitride under visible light irradiation: experimental and theoretical studies, New J. Chem. 44 (22) (2020) 9238–9247.

[52] M.G. Kim, J.M. Kang, J.E. Lee, K.S. Kim, K.H. Kim, M. Cho, S.G. Lee, Effects of calcination temperature on the phase composition, photocatalytic degradation, and virucidal activities of TiO_2 nanoparticles, ACS Omega 6 (16) (2021) 10668–10678.

[53] B. Bharti, H. Li, D. Liu, H. Kumar, V. Manikandan, X. Zha, F. Ouyang, Efficient Zr-doped FS–TiO_2/SiO_2 photocatalyst and its performance in acrylonitrile removal under simulated sunlight, Appl. Phys. A Mater. Sci. Process 126 (11) (2020) 1–10.

[54] D. Liu, Z. Wu, F. Tian, B.C. Ye, Y. Tong, Synthesis of N and La co-doped TiO_2/AC photocatalyst by microwave irradiation for the photocatalytic degradation of naphthalene, J. Alloys Compd. 676 (2016) 489–498.

[55] W. Wu, S. Liang, Y. Chen, L. Shen, R. Yuan, L. Wu, Mechanism and improvement of the visible light photocatalysis of organic pollutants over microcrystalline $AgNbO_3$ prepared by a sol-gel method, Mater. Res. Bull. 48 (4) (2013) 1618–1626.

[56] D. Wang, T. Kako, J. Ye, Efficient photocatalytic decomposition of acetaldehyde over a solid-solution perovskite $(Ag_{0.75}Sr_{0.25})(Nb_{0.75}Ti_{0.25})O_3$ under visible-light irradiation, J. Am. Chem. Soc. 130 (9) (2008) 2724–2725.

[57] P.M. Wood, The potential diagram for oxygen at PH 7, Biochem. J. 253 (1) (1988) 287–289.